

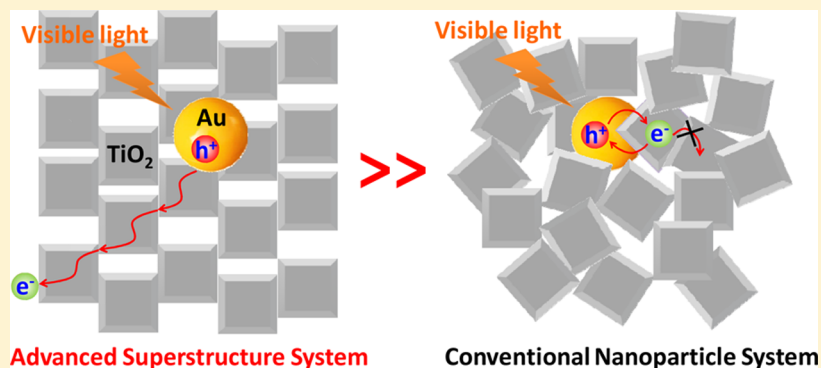
Au/TiO₂ Superstructure-Based Plasmonic Photocatalysts Exhibiting Efficient Charge Separation and Unprecedented Activity

Zhenfeng Bian,[†] Takashi Tachikawa,^{*,†,‡} Peng Zhang,[†] Mamoru Fujitsuka,[†] and Tetsuro Majima^{*,†}

[†]The Institute of Scientific and Industrial Research (SANKEN), Osaka University, Mihogaoka 8-1, Ibaraki, Osaka 567-0047, Japan

[‡]PRESTO, Japan Science and Technology Agency (JST), 4-1-8 Honcho Kawaguchi, Saitama 332-0012, Japan

S Supporting Information



ABSTRACT: Plasmonic photocatalysts were successfully synthesized by the modification of TiO₂ mesocrystals with Au nanoparticles (NPs) by a simple impregnation method. The Au NP sensitizers show a strong photoelectrochemical response in the visible-light region (400–800 nm) due to their surface plasmon resonance (SPR). The diffuse reflectance spectroscopy measurements on a wide range of time scales (from picoseconds to minutes) demonstrate that a substantial part of electrons, injected from the Au NPs to the TiO₂ mesocrystals through the SPR excitation, directionally migrate from the basal surfaces to the edges of the plate-like mesocrystals through the TiO₂ nanocrystal networks and are temporally stored there for further reactions. This anisotropic electron flow significantly retarded the charge recombination of these electrons with the holes in the Au NPs, thereby improving the visible-light-photocatalytic activity (for organic-pollutant degradation) by more than an order of magnitude, as compared to that of conventional Au/TiO₂ NP systems.

INTRODUCTION

Photocatalysis based on semiconductor technology has attracted much attention for effective utilization of solar energy in environmental purification, organic synthesis (e.g., selective oxidation or reduction), and water splitting for hydrogen generation.^{1–3} Recently, the incorporations of plasmonic gold (Au) or silver (Ag) nanoparticles (NPs) onto wide-bandgap semiconductors such as titanium dioxide (TiO₂) and cerium dioxide (CeO₂) have been shown to enhance the photocatalytic activity in the visible region due to the strong surface plasmon resonance (SPR) excitation of such metal NPs.^{4–10} SPR arises from the collective oscillations of the surface electrons on metal NPs, and the hot electrons have been shown to be injected into the conduction band of the semiconductor over the Schottky barrier.^{11–13} However, the fast charge recombination between the injected electrons in semiconductor NPs and the holes in Au NPs (mostly completed within 1 ns for Au/TiO₂^{12,13}) significantly reduced the probability for subsequent chemical reactions, which is directly related to their photocatalytic and photovoltaic performance.

The main focus in the synthesis of semiconductor-based plasmonic photocatalysts has been to precisely control the

shapes and sizes of the metal NPs.^{14–19} The structural and electronic properties of semiconductor materials should also be essential for achieving the proper function of such composite catalysts. We have recently demonstrated that the anatase TiO₂ mesocrystal (MesoTiO₂) superstructures significantly enhance the charge separation upon UV-light irradiation, resulting in remarkably long-lived charges, and thereby exhibit significant enhancement in photoconductivity and photocatalytic activities.^{20,21} Single-particle-level observations verified that the electron transport within MesoTiO₂ superstructures reaches up to micrometer distance.²¹ However, the compatibility of MesoTiO₂ superstructures with plasmonic metal NPs has not yet been reported. In this Article, we have answered the central question: “Does the semiconductor superstructure assist the migration of the electrons injected from the excited Au NPs and thereby enhance the visible-light-induced photocatalytic activity?” In this study, a simple impregnation method was used to deposit Au NPs on various TiO₂ materials. As compared to the conventional NP systems, the superstructure-based Au/

Received: November 1, 2013

Published: December 5, 2013

MesoTiO₂ system was found to significantly enhance the visible-light photocatalytic activity (more than an order of magnitude). Furthermore, the SPR-induced electron injection, trapping, recombination, and accumulation processes were thoroughly investigated by monitoring the specific photoabsorption of the electrons in TiO₂ using time-resolved diffuse reflectance spectroscopy.

■ EXPERIMENTAL DETAILS

Preparation of TiO₂. MesoTiO₂ was prepared from a precursor solution of NH₄F (Wako Pure Chemical Industries), TiF₄ (Sigma-Aldrich), H₂O, NH₄NO₃ (Wako Pure Chemical Industries), and P123 (Sigma-Aldrich, amphiphilic triblock copolymer PEO–PPO–PEO ((EO)₂₀(PO)₇₀(EO)₂₀)) (molar ratio = 232:93:32 000:453:1). The above precursors were placed on a silicon wafer to form a thin layer. The thickness of the aqueous solution layer should be no more than 1 mm before annealing. The precursor solution was calcined in air using a heating rate of 10 °C min⁻¹ at 500 °C for 2 h. Furthermore, the obtained samples were calcined at the same temperature in oxygen atmosphere for 8 h to completely remove surface residue. NanoTiO₂ was synthesized according to the literature,²⁰ and annealed at 500 °C in oxygen atmosphere for 8 h.

Preparation of Colloidal Solutions of Au NPs. A solution of HAuCl₄·3H₂O (Aldrich, 2 mL, 1 wt %) was dissolved in 99 mL of Milli-Q ultrapure water (Millipore) in a three-neck round-bottom flask and heated to 100 °C. Under vigorous stirring, sodium citrate (Wako Pure Chemical Industries, 1.2 mL, 1 wt %) was added, and the reaction mixture was maintained at the boiling temperature for further 30 min before being cooled to room temperature. Finally, the colloidal solution of Au NPs was obtained.

Preparation of Au/TiO₂. Twenty milliliters Au colloidal solution was mixed with 10 mg of TiO₂ and sonicated for 2 min. This suspension was heated to evaporate the solvent at 100 °C and then calcined in air using a heating rate of 10 °C min⁻¹ at 500 °C for 0.5 h. The samples were again dispersed in water, sonicated in an ultrasonic bath, and centrifuged at 10 000 rpm (Hitachi, himac CF16RX) to remove the weakly attached Au NPs. The solid products were then dried at 100 °C.

Preparation of Au/MesoTiO₂-PD. 0.25 g of MesoTiO₂, 225 mL of Milli-Q ultrapure water (Millipore), 25 mL of methanol, and 9.6 mol % HAuCl₄ (Sigma-Aldrich) were mixed to form a homogeneous suspension. The solutions were then exposed to UV light from a mercury light source (Asahi Spectra, REX-120) for 30 min at room temperature. Finally, the solutions were centrifuged at 10 000 rpm to separate the solid products. The products were subsequently calcined in air at 500 °C for 30 min.

Preparation of Pt/TiO₂. Pt/TiO₂ was prepared by the photochemical deposition (PD) method as described in the literature.²¹ In a typical synthesis, 0.25 g of TiO₂ (MesoTiO₂ or P25), 225 mL of Milli-Q ultrapure water, 25 mL of methanol, and H₂PtCl₆ (Sigma-Aldrich) were mixed forming a homogeneous suspension. The solutions were then exposed to UV light for 30 min at room temperature. Finally, the solutions were centrifuged at 10 000 rpm to separate the solid products. The products were subsequently calcined in air (20 °C min⁻¹) at 300 °C for 30 min. The amounts of loaded Pt were determined by inductively coupled plasma (ICP) emission spectroscopy (Shimadzu, ICPS-8100).

Characterization of Materials. The samples were characterized using X-ray diffraction (Rigaku, Smartlab; operated at 40 kV and 200 mA, Cu K α source), scanning electron microscopy (SEM) (Jeol, JSM-6330FT), transmission electron microscopy (TEM) (Jeol, JEM 3000F; operated at 300 kV or Hitachi, H-800; operated at 200 kV), and nitrogen sorption (BEL Japan, BEL-SORP max). The Brunauer–Emmett–Teller (BET) method was utilized to calculate the specific surface area. The pore volume and pore diameter distribution were derived from the adsorption isotherms by the Barrett–Joyner–Halenda (BJH) model.

Steady-State Diffuse Reflectance Spectral Measurement. The steady-state UV–vis diffuse reflectance spectra were measured

using UV–vis–NIR spectrophotometers (Jasco, V-570) at room temperature. The Kubelka–Munk function, $F(R_{\infty})$, is calculated from the equation: $F(R_{\infty}) = (1 - R_{\infty})^2/2R_{\infty}$, where R_{∞} is the absolute reflectance of the sample relative to the standard material (Labsphere, Spectralon).

Photocatalytic Activity Tests. For typical photocatalytic runs, 4 mL of TiO₂ dispersion (1.0 g L⁻¹) containing aqueous solution (methylene blue (MB), 1.0 × 10⁻⁵ M; rhodamine B (RhB), 1.0 × 10⁻⁵ M) was sonicated for 5 min, and then transferred into a quartz cuvette. The percentages of preadsorbed substrates in aqueous suspensions of TiO₂ before visible-light irradiation were below 5% of total amount under equilibrium conditions. The photocatalytic reaction was initiated by a Xe light source (Asahi Spectra, LAX-C100) through the filters (460 nm < λ < 700 nm) at room temperature. The intensity of the visible light was measured to be about 500 mW cm⁻². The reaction time was 20 min for MB and 2 min for RhB, while it was 3 h for 4-chlorophenol (4-CP). After the visible illumination was stopped, the sample was centrifuged at 10 000 rpm (Hitachi, himac CF16RX) to remove the particles. The concentration of unreacted molecules was analyzed by a UV–vis spectrophotometer (Shimadzu, UV-3100) at the characteristic wavelength, from which the degradation yield was calculated.

Photocurrent Experiments. Photocurrent data were measured using a mercury light source (REX-120). Amperometric $i-t$ curve and linear sweep voltammetry experiments were carried out at room temperature using an electrochemical analyzer (ALS, model 660A).

Time-Resolved Diffuse Reflectance Measurements. The femtosecond transient absorption spectra were measured by the pump and probe method using a regeneratively amplified titanium sapphire laser (Spectra-Physics, Spitfire Pro F, 1 kHz) pumped by a Nd:YLF laser (Spectra-Physics, Empower 15). The seed pulse was generated by a titanium sapphire laser (Spectra-Physics, MaiTai VFSJ-W; fwhm 80 fs) pumped with a diode-pumped solid-state laser (Spectra-Physics, Millennia VIII). An optical parametric amplifier (Spectra Physics, OPA-800CF-1) was used to produce the excitation pulse (530 nm; 2.2 μ J). The excitation light was depolarized. A white light continuum pulse, which was generated by focusing the residual of the fundamental light on a sapphire crystal after the computer-controlled optical delay, was divided into two parts and used as the probe and the reference lights, of which the latter was used to compensate the laser fluctuation. Both the probe and the reference lights were directed to the sample cell, and the reflected lights were detected by a linear InGaAs array detector equipped with the polychromator (Solar, MS3504). The pump pulse was chopped by the mechanical chopper synchronized to one-half of the laser repetition rate, resulting in a pair of spectra with and without the pump, from which the absorption change induced by the pump pulse was estimated. All measurements were carried out at room temperature.

Hydrogen Production Activity Tests. The catalyst powder (50 mg) was suspended in 50 vol % 2-propanol/water (5 mL), bubbled with Ar, and sealed with a rubber septum. For visible-light hydrogen production, the suspensions were irradiated with visible light (Asahi Spectra, HAL-C100; 460–700 nm, 200 mW cm⁻²) with magnetic stirring at room temperature. A 460 nm cutoff filter and a cold filter (Asahi Spectra, SC0751) were used to remove UV and near-infrared light. The amount of H₂ in the gas phase was measured using a Shimadzu GC-8A gas chromatograph equipped with an MS-5A column and a thermal conductivity detector (TCD).

■ RESULTS AND DISCUSSION

The structures of the MesoTiO₂ and Au/MesoTiO₂ systems were characterized by SEM and TEM analyses. The pure MesoTiO₂ system shows a plate-like structure with 3–5 μ m size and 100–300 nm thickness (Figure 1a). The MesoTiO₂ system consists of anatase TiO₂ nanocrystals with ~22 nm diameter (obtained from the Scherrer analysis of X-ray diffraction) (Supporting Information Figure S1), and it has porous structures with a high surface area of 96 m² g⁻¹ and ~11

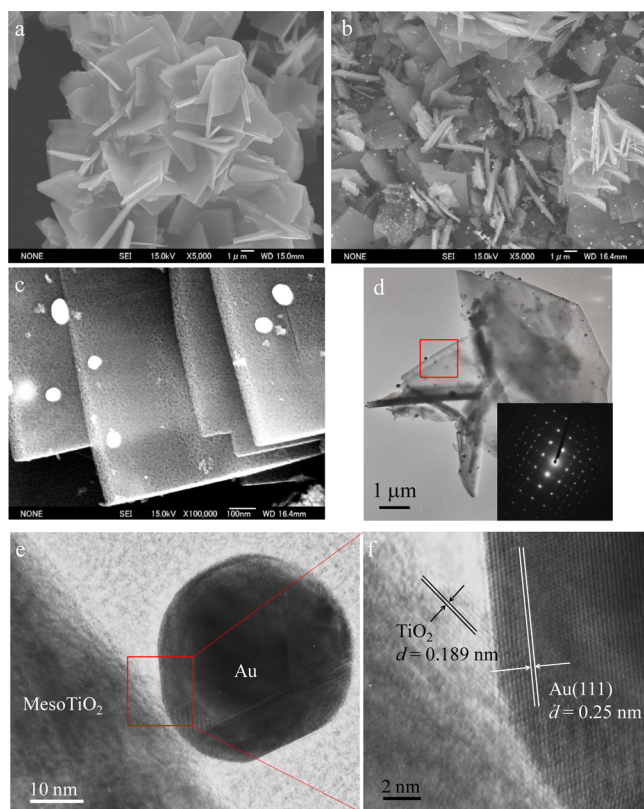


Figure 1. SEM images of (a) MesoTiO₂ and (b,c) Au/MesoTiO₂. (d) TEM image of Au/MesoTiO₂. Inset indicates a SAED pattern. (e,f) HRTEM images of Au/MesoTiO₂.

nm pore size (obtained from the Brunauer–Emmett–Teller and Barrett–Joyner–Halenda analyses, respectively) (Supporting Information Figure S2). During the thermal treatment with the Au NP colloidal solutions, the structural features of the MesoTiO₂ system remain constant except for the bright spots of the Au NPs on the MesoTiO₂ surface, as seen in the SEM image (Figure 1b). The porous surface structure of the Au/MesoTiO₂ system is clearly seen from a high-resolution field emission SEM image (Figure 1c), where the Au NPs are visible as bright particles. The Au NPs are mostly located on the basal surfaces of MesoTiO₂ due to their stochastic nature (~20 Au NPs per MesoTiO₂), and their size is ~50 nm with size distribution lying between 30 and 80 nm (Supporting Information Figure S3a). The TEM analysis also shows that the Au NPs (black spots) are homogeneously loaded onto the surface of the MesoTiO₂ system (Figure 1d). A selected area electron diffraction (SAED) pattern recorded on Au/MesoTiO₂ (the red square in Figure 1d) shows a diffraction pattern corresponding to single-crystal anatase along the [001] zone axis (inset of Figure 1d). High-resolution TEM (HRTEM) images taken from a part of the Au/MesoTiO₂ system show the detailed structures of the composite (Figure 1e and f). Both the MesoTiO₂ and the Au NPs are highly crystallized, as evidenced by the well-resolved Au(111) (0.25 nm) and TiO₂(001) (0.189 nm) crystalline lattices (Figure 1f); a close contact between them is advantageous for electron transfer from the excited Au NPs to the MesoTiO₂ system.²²

To understand the photocatalytic properties of the Au/MesoTiO₂ system, three reference samples were selected: (i) Au/MesoTiO₂-PD (photochemical deposition), (ii) Au/NanoTiO₂, and (iii) Au/P25 systems (Supporting Information

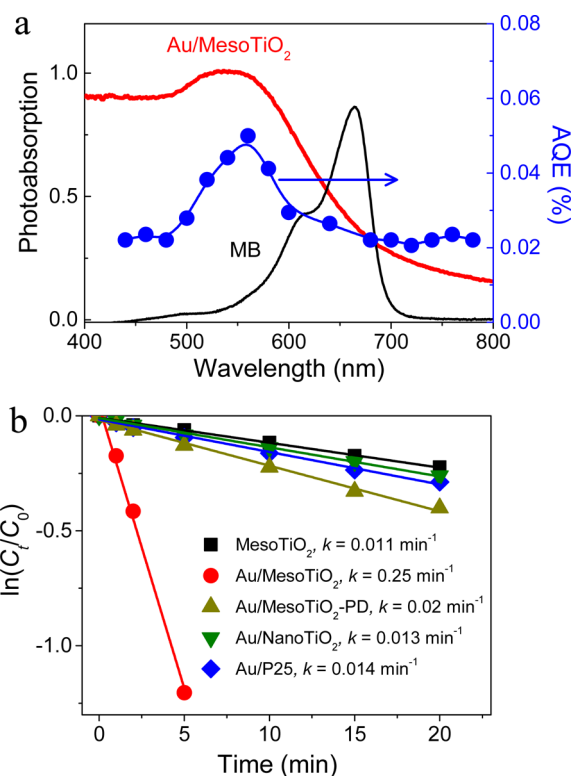


Figure 2. (a) AQE (right axis, blue line) and SPR spectra (left axis, red line) of the Au/MesoTiO₂ system in photocatalytic degradation of MB and visible absorption spectrum of MB (black line). (b) Kinetic linear fitting curves for liquid-phase photocatalytic degradation of MB over different samples under visible-light irradiation (460–700 nm).

Figures S3 and S4). The Au/MesoTiO₂-PD system is prepared by the PD method; most of the Au NPs are located on the lateral surfaces of MesoTiO₂.²¹ The NanoTiO₂ system comprises an anatase nanocrystal with truncated bipyramidal morphology (18 nm particle size and 41 m² g⁻¹ surface area), which is an analogue of the TiO₂ nanocrystal building blocks of the MesoTiO₂ superstructure.²⁰ P25 TiO₂ consists of both the anatase and the rutile crystalline phases and is frequently used as the benchmark in photocatalysis (19 nm particle size and 55 m² g⁻¹ surface area).²⁰

First, the optical properties of the Au/MesoTiO₂ system as well as that of the reference samples were examined by steady-state UV–visible diffuse reflectance spectroscopy (Supporting Information Figure S5). The bare MesoTiO₂ system had no absorption in the visible region (400–800 nm). After loading the Au NPs onto the MesoTiO₂ system, a new absorption band appeared at around 535 nm, which can be ascribed to the SPR excitation of the Au NPs.^{23–25} The PD sample (Au/MesoTiO₂-PD) has a broader and red-shifted absorption peak due to the uniformity of Au NPs (~20–90 nm size distribution). The Au/NanoTiO₂ and Au/P25 samples showed the absorption peaks at around 542 and 548 nm, respectively. Because the size distributions of Au NPs in the different samples are very similar (Supporting Information Figure S3), the red shifts of the Au/NanoTiO₂ and Au/P25 systems are possibly due to the densely attached TiO₂ NPs having a high refractive index, as compared to that of air used as the medium, surrounding the Au NPs.^{23–26}

The photocatalytic degradation of MB in an aqueous phase was selected as the probe reaction to verify whether the activity

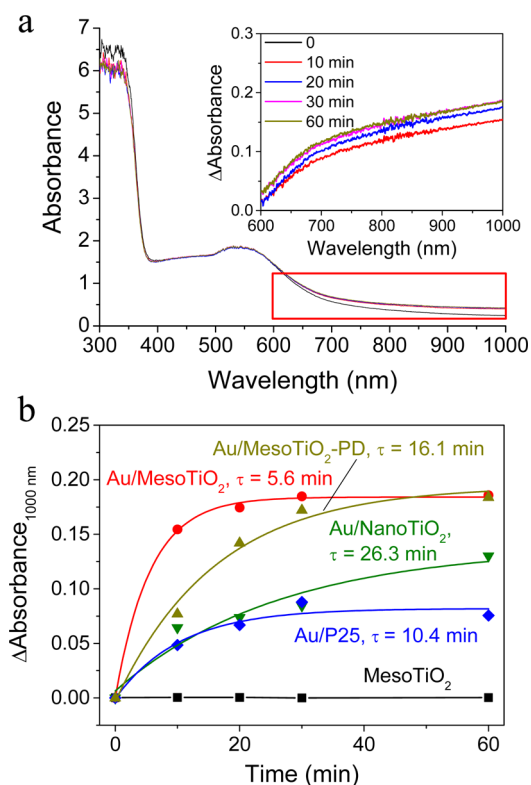


Figure 3. (a) Diffuse reflectance spectra of Au/MesoTiO₂ system in Ar-saturated methanol during visible-light irradiation (460–700 nm and 500 mW cm⁻²). Inset shows differential spectra. (b) Time evolution of maximum absorbance measured at 1000 nm wavelength under visible-light irradiation.

was due to the SPR excitation of Au NPs or the sensitization of the dye molecules.^{27,28} The MB degradation study in an aqueous suspension of the Au/MesoTiO₂ system was carried out at 298 K under the irradiation of monochromatic visible light with a width of ± 5 nm and intensity of 9.6 mW cm⁻². The apparent quantum efficiency (AQE) at each centered wavelength of the monochromatic light was calculated from the ratio of the number of decomposed MBs to those of the irradiated photons by using the following expression: $AQE = (\text{number of decomposed MBs} / \text{number of incident photons}) \times 100\%$.²⁹ As shown in Figure 2a, the action spectrum of the AQE is in agreement with the SPR spectrum of the Au/MesoTiO₂ system, while it is completely different from the photoabsorption feature of the MB. The AQE of the Au/MesoTiO₂ system reached 0.050% at 560 nm and 0.022% at 780 nm under the above conditions. The photoabsorption of MB is more intense than the surface plasmon absorption in the wavelength range over 600 nm (Figure 2a and Supporting Information Figure S6). The observed action spectrum might be partially distorted by the optical filter effect. Another dye molecule RhB showed an action spectrum similar to that obtained for MB (Supporting Information Figure S7). The AQE of the Au/MesoTiO₂ system reached 0.11% at 560 nm and 0.018% at 780 nm during the photodegradation of RhB dye. Therefore, it can be concluded that the dye degradation was mainly induced by the SPR excitation of the Au NPs.

The incident-photon-to-current-efficiency (IPCE) spectrum of the Au/MesoTiO₂ system coated on an indium–tin–oxide (ITO) electrode under the monochromatic visible-light irradiation was further measured (Supporting Information

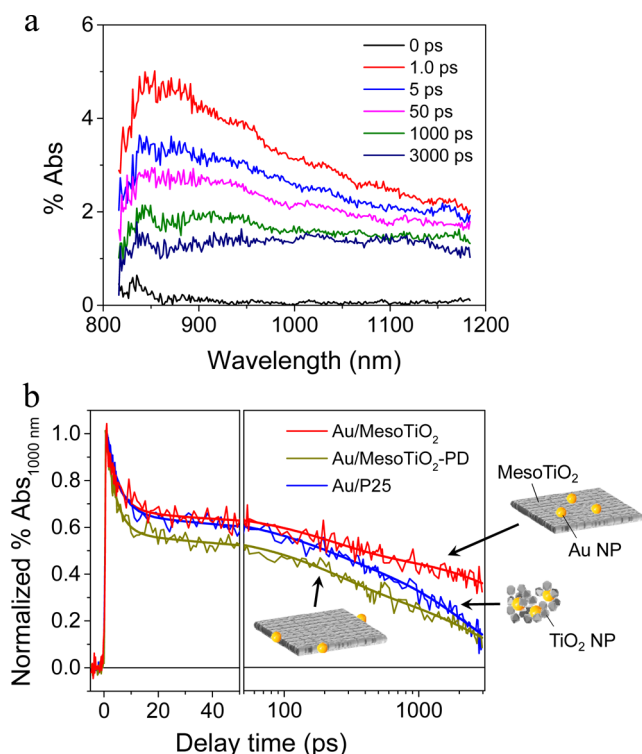


Figure 4. (a) Time-resolved diffuse reflectance spectra observed after 530-nm laser flash photolysis of Au/MesoTiO₂ in ambient air. (b) Normalized transient absorption traces observed at 1000 nm for Au/MesoTiO₂ (red), Au/MesoTiO₂-PD (dark yellow), and Au/P25 (blue) systems. Bold lines indicate multiexponential curves fitted to kinetic traces.

Figure S8). The shape of this IPCE spectrum closely resembles that of the SPR absorption spectrum of the Au/MesoTiO₂ system in addition to the response of TiO₂, suggesting that the observed photocurrents originate from the SPR excitation of the Au NPs. The increase of the IPCE toward the shorter wavelength region below ~ 510 nm also infers the involvement of the interband transition as discussed elsewhere.^{15,26}

To evaluate the photocatalytic activity of different samples, the photocatalytic aqueous-phase oxidations of MB, RhB, and 4-CP were examined (Figure 2b and Supporting Information Figure S9). No photocatalytic degradation was observed even after 3 h under the dark or no photocatalyst conditions. A very low photocatalytic degradation of the MB dye was observed on pure MesoTiO₂ (AQE = 0.00015%), Au/MesoTiO₂-PD (0.00028%), Au/NanoTiO₂ (0.00018%), and Au/P25 (0.00020%) systems after visible-light irradiation (460–700 nm, 500 mW cm⁻²) for 20 min, while the Au/MesoTiO₂ system displayed complete decolorization of MB within 10 min (0.0035%) (Figure 2b). The plasmonic Au nanostructures are considered as good thermocatalysts for various chemical reactions.^{30–32} The temperature of the Au/MesoTiO₂ suspension increased by 2–3 °C after visible-light irradiation (460–700 nm, 500 mW cm⁻²) for 10 min (environmental temperature was 25 °C). Thus, the thermal catalytic effect on the degradation is likely to be small. On the basis of a simplified Langmuir–Hinshelwood model,²⁰ the apparent first-order-rate constant (k) for the photocatalytic degradation of MB was calculated to be 0.25 min⁻¹ for the Au/MesoTiO₂ system, which is much higher than that of pure MesoTiO₂ (0.011 min⁻¹), Au/MesoTiO₂-PD (0.020 min⁻¹), Au/NanoTiO₂

Table 1. Kinetic Parameters of Decays Observed for Au/TiO₂ Samples

sample	τ_1 (ps)	τ_2 (ps)	τ_3 (ps)
Au/MesoTiO ₂	4.5 ± 0.5 (16%)	210 ± 40 (22%)	9600 ± 1600 (62%)
Au/MesoTiO ₂ -PD	3.8 ± 0.3 (51%)	210 ± 30 (19%)	2900 ± 260 (30%)
Au/P25	4.6 ± 0.4 (30%)	160 ± 30 (17%)	2300 ± 250 (53%)

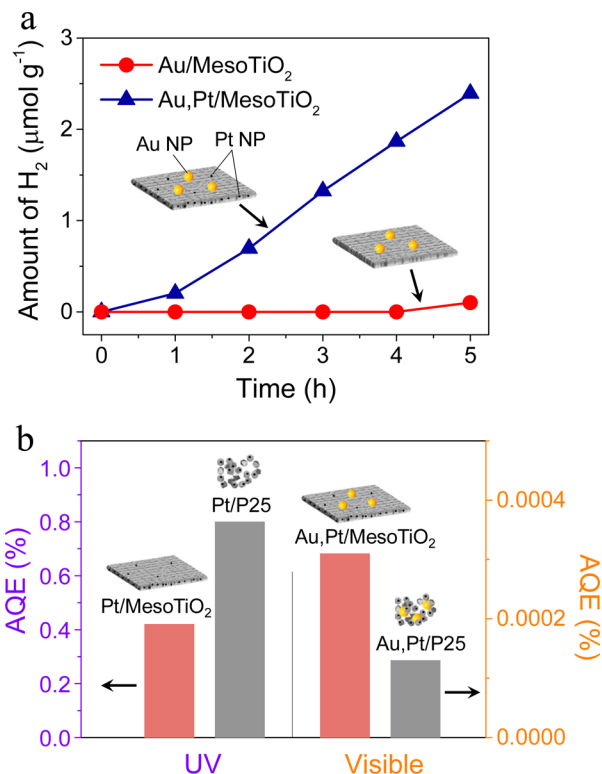


Figure 5. (a) Time-dependent profiles of hydrogen production in the visible light-illuminated 50 vol % 2-propanol/water suspensions of Au/MesoTiO₂ and Au,Pt/MesoTiO₂. 2-Propanol serves as a sacrificial reagent. (b) Comparison of hydrogen production performance under UV and visible-light irradiation. The same amount of Pt (1.0 wt %) was loaded on the catalyst surface. The synthesis procedures and structures of the Pt-loaded samples are described in ref 20. The AQE for hydrogen evolution is calculated by using the following expression: $AQE = (2 \times \text{number of evolved H}_2 / \text{number of incident photons} \times 100\%)$.²⁹

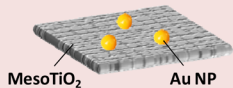
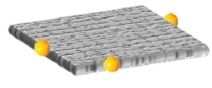
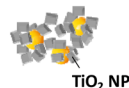
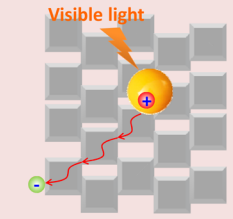
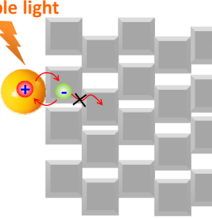
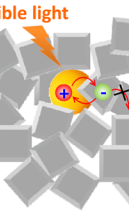
(0.013 min⁻¹), and Au/P25 (0.014 min⁻¹) systems. The photocatalytic degradation of the other probes such as RhB and 4-CP compounds showed similar trends (Supporting Information Figure S9). Thus, it can be concluded that the Au NPs on the MesoTiO₂ system yield more than 1 order of magnitude of enhancement in the visible-light photocatalytic activity.

It is well-known that reduced TiO₂ absorbs both visible light and near-infrared light.³³ Figure 3a shows the steady-state diffuse reflectance spectra observed for the Au/MesoTiO₂ powders immersed in Ar-saturated methanol (effective scavenger for holes in Au NPs⁴) before and after visible-light irradiation. The absorbance in the 600–1000 nm wavelength range clearly increased, suggesting that the electrons accumulated in the MesoTiO₂ system.³³ The time evolution of the maximum absorbance at 1000 nm wavelength for different samples is shown in Figure 3b. Pure MesoTiO₂ system showed no visible-light absorption at 1000 nm before and after the visible-light irradiation. On the other hand, the Au/MesoTiO₂ system exhibits a significant enhancement in visible-light

absorption, and the time constant for growth is estimated to be 5.6 min from a single-exponential fitting. The time constants for the Au/NanoTiO₂ and Au/P25 systems are 26.3 and 10.4 min, respectively, which are much less than that for the Au/MesoTiO₂ system. Moreover, the concentration of the stored electrons in the MesoTiO₂ system, which might be dependent on the surface area, is about 2 times higher than those in the NanoTiO₂ and P25 systems. The time constant for the Au/MesoTiO₂-PD system is 16.1 min, and its maximum electron concentration is similar to that in the Au/MesoTiO₂ system. This finding is very interesting because the Au/MesoTiO₂ and Au/MesoTiO₂-PD systems have the same amounts of Au loading and similar size of Au particles. The crucial difference in these two systems is in the locations of Au NPs on the surface of MesoTiO₂: the Au NPs are mainly located on the basal surfaces of the Au/MesoTiO₂ system, whereas they are present on the lateral surfaces in the Au/MesoTiO₂-PD system (Supporting Information Figure S4c), which correspond to anatase {001} and {101} facets, respectively.^{20,21} The injected electrons are inclined to migrate from the basal surfaces to the edges of the MesoTiO₂ system because of the crystal-face-dependent electron trapping probability,^{21,34} thus inhibiting the charge recombination process between the electrons in MesoTiO₂ and the holes in Au NPs. In addition, the electronic repulsive forces induced by the stored electrons on the anatase{101} facets might prohibit electron injection from the Au NPs located on the lateral surfaces of MesoTiO₂.

Time-resolved diffuse reflectance spectroscopy, a powerful analytical tool for investigating ultrafast processes in photocatalysis under various conditions,^{35,36} was employed to measure the lifetime of the injected electrons, which in turn provides the direct evidence for electron transfer from the excited Au NPs to the modified TiO₂. Immediately after the 530-nm laser excitation of the Au/TiO₂ samples (80 fs pulse width and 2.2 μJ pump intensity), a broad absorption band appeared in the whole wavelength region (Figure 4a and Supporting Information Figure S10). The transient absorption spectrum of reduced TiO₂ is considered to be superimposed with that of the trapped electrons (600–1000 nm) and free electrons (increasing monotonically from the visible to near-infrared regions).^{36,37} Further, it was observed that electron injection from the excited Au NPs to the TiO₂ system takes place within a subpicosecond time scale, which is consistent with the reports in the literature.^{12,13} For a time period of 1.0–3000 ps, the concentration of the electrons in the TiO₂ system decreased in a multiexponential fashion due to the charge recombination of these electrons with the holes in the Au NPs, because the other relaxation/deactivation pathways such as surface trapping (<200 fs for 20 nm TiO₂ NPs³⁸) and electron transfer to oxygen molecules (μs–ms³⁹) occur on different time scales. At 3000 ps, the surviving electron concentration in the Au/MesoTiO₂ system is ~36% of the maximum. For the Au/P25 and Au/MesoTiO₂-PD systems, the remaining electrons were determined to be <15%. Moreover, the concentration of the trapped electrons (800–1000 nm) decreased faster than that of the free electrons (1000–1200 nm) (Figure 4a and

Table 2. Visible-Light Photocatalytic Activity of Au/TiO₂ Systems

system	Au/MesoTiO ₂	Au/MesoTiO ₂ -PD	Au/TiO ₂ NP (Au/NanoTiO ₂ , Au/P25)
structure			
electron transfer process			
AQE for MB degradation, % ^a	0.0035	0.00028	0.00018–0.00020
electron accumulation time, min ^b	5.6	16	10–26
electron lifetime, ns (relative amplitude, %) ^c	9.6 (62)	2.9 (30)	2.3 (53)
surviving electron concentration at 3 ns, % ^c	36	12	14
AQE for H ₂ formation, % ^d	0.00031	NA	0.00013

^aObtained under 460–700 nm light irradiation (500 mW cm⁻²) (Figure 2b). ^bObtained by steady-state diffuse reflectance measurements (Figure 3). ^cObtained by time-resolved diffuse reflectance measurements (Figure 4). ^dObtained under 460–700 nm light irradiation (200 mW cm⁻²) (Figure 5b). Pt NPs (1 wt %) were loaded on the surface by the PD method.

Supporting Information Figure S10). This phenomenon was observed for the first time and implies a fast charge recombination between the trapped electrons in TiO₂ and the holes in Au NPs prior to diffusing away from the vicinity of the Au NPs. Figure 4b shows the normalized transient absorption traces of electrons probed at 1000 nm. The transient absorption trace on the Au/MesoTiO₂ system was fitted to a three-exponential function with time constants of 4.5 ps (16%), 210 ps (22%), and 9600 ps (62%) (Table 1). The repeated experiments produced the same results, thereby eliminating the possibility of sample damage by repetitive laser irradiation. In the same manner, for the Au/P25 system, three decay-time components are obtained: (i) 4.6 ps (30%), (ii) 160 ps (17%), and (iii) 2300 ps (53%), which indicate the faster charge recombination process. The slower two components are similar to the reported values for the Au/TiO₂ NPs (probed at 3440 nm, where only free electrons absorbed energy).¹³ It is noteworthy that, as compared to the Au/MesoTiO₂ system, the Au/MesoTiO₂-PD system also exhibited shortened electron lifetimes (3.8 ps (51%), 210 ps (19%), and 2900 ps (30%)). Because most of the Au NPs on the Au/MesoTiO₂-PD system were located on the lateral surfaces, the injected electrons readily recombine with the holes in the Au NPs. Meanwhile, the Au NPs on the basal surfaces of the plate-like MesoTiO₂ system extend the lifetime of the electrons due to the anisotropic electron flow from the center to the edge, thus retarding the charge recombination process. Therefore, the Au/MesoTiO₂ system could significantly enhance the visible-light photocatalytic activity.

The site-selective loading of Pt NPs, which are commonly used as a cocatalyst for hydrogen production,²⁹ on Au/

MesoTiO₂ is expected to further improve its photocatalytic performance. To this end, we photochemically deposited Pt NPs preferentially on the lateral surfaces of MesoTiO₂,²¹ prior to the loading of Au NPs on the basal surfaces (Au,Pt/MesoTiO₂) and evaluated the hydrogen production under visible-light irradiation (460–700 nm, 200 mW cm⁻²) using a gas chromatograph equipped with TCD. The amounts of deposited Pt were 1 wt %, and the sizes of Pt NPs are approximately 3.5 and 2.8 nm for Pt/MesoTiO₂ and Pt/P25, respectively (Supporting Information Figure S11).²¹ As shown in Figure 5a, the Au,Pt/MesoTiO₂ system exhibited a low but measurable visible-light activity, while no hydrogen was produced in the absence of Pt loading. To compare the photocatalytic performance between superstructure and nanoparticle systems, we examined the inherent hydrogen production ability of Pt/MesoTiO₂ and Pt/P25 under UV light irradiation (365 nm, 100 mW cm⁻²). The AQEs for hydrogen production are 0.42% and 0.80% for Pt/MesoTiO₂ and Pt/P25, respectively (Figure 5b and Supporting Information Figure S12). The lower activity of Pt/MesoTiO₂ is partially attributable to the fact that anatase {001} facets, which are dominant in MesoTiO₂, are less active than {101} facets for hydrogen evolution.^{40,41} Therefore, as demonstrated in Figure 5b, the superior visible-light activity of Au,Pt/MesoTiO₂ (AQE = 0.00031%) than Au,Pt/P25 (0.00013%) supports our hypothesis that the injected electrons from the excited AuNPs can efficiently migrate to the catalytic sites located on the edge of MesoTiO₂ through the nanocrystal networks.

CONCLUSION

We have studied the visible-light photocatalytic activity of mesocrystalline TiO₂ superstructures modified with plasmonic Au NPs on specific surfaces (e.g., basal and lateral surfaces). As summarized in Table 2, the visible-light photocatalytic activity of the Au/MesoTiO₂ sample was more than 10 times that of the conventional NP-based composites, that is, Au/NanoTiO₂ and Au/P25 systems. By using time-resolved diffuse reflectance spectroscopy, the subsequent reaction dynamics of the injected electrons (from the excited Au NPs to the TiO₂ system) could be investigated. The time constant for electron accumulation in the Au/MesoTiO₂ system (5.6 min) is significantly shorter than those (10–26 min) in the Au/MesoTiO₂-PD and Au/TiO₂ NP systems. This finding was further supported by the fact that >60% electrons in the Au/MesoTiO₂ system have prolonged electron lifetime of ~10 ns in ambient air, whereas the electrons in the Au/MesoTiO₂-PD and Au/P25 TiO₂ systems recombine with the holes in the Au NPs within a few nanoseconds. As compared to the Au/MesoTiO₂-PD system, where the Au NPs are mostly located on the lateral surfaces of MesoTiO₂, it can be concluded that the electrons injected from the excited Au NPs on the basal surfaces of MesoTiO₂ are effectively delivered to the lateral surfaces of the crystal through the TiO₂ nanocrystal networks. This significantly retards the charge recombination process of the electrons (with the holes in the Au NPs), thus enhancing the visible-light photocatalytic performance for organics degradation and hydrogen production. Such an outstanding feature allows for reduced consumption of the metal loading on the semiconductor, which is especially advantageous for near-infrared active metallic nanostructures with larger sizes (e.g., Au nanorods). We believe that our findings in this study will create new avenues for the design and synthesis of efficient and economical plasmonic photocatalysts with potential applications in solar-energy conversion.

ASSOCIATED CONTENT

Supporting Information

Additional results of structural characterizations and photocatalytic activity tests of the samples. This material is available free of charge via the Internet at <http://pubs.acs.org>.

AUTHOR INFORMATION

Corresponding Authors

tachi45@sanken.osaka-u.ac.jp

majima@sanken.osaka-u.ac.jp

Notes

The authors declare no competing financial interest.

ACKNOWLEDGMENTS

We thank Prof. Kamegawa and Prof. Yamashita, Osaka University, for nitrogen sorption and hydrogen evolution measurements. A part of the TEM observation was carried out in a facility at the Research Center for Ultrahigh Voltage Electron Microscopy, Osaka University. T.T. thanks the Asahi Glass Co., Ltd., for financial support. T.M. thanks the WCU (World Class University) program through the National Research Foundation of Korea funded by the Ministry of Education, Science and Technology (R31-10035) for support. This work has been partly supported by a Grant-in-Aid for Scientific Research (Projects 25220806, 25810114, and others)

from the Ministry of Education, Culture, Sports, Science and Technology (MEXT) of the Japanese Government.

REFERENCES

- (1) Chen, X. B.; Shen, S. H.; Guo, L. J.; Mao, S. S. *Chem. Rev.* **2010**, *110*, 6503–6570.
- (2) Fujishima, A.; Zhang, X. T.; Tryk, D. A. *Surf. Sci. Rep.* **2008**, *63*, 515–582.
- (3) Maeda, K.; Domen, K. *J. Phys. Chem. Lett.* **2010**, *1*, 2655–2661.
- (4) Tian, Y.; Tatsuma, T. *J. Am. Chem. Soc.* **2005**, *127*, 7632–7637.
- (5) Awazu, K.; Fujimaki, M.; Rockstuhl, C.; Tominaga, J.; Murakami, H.; Ohki, Y.; Yoshida, N.; Watanabe, T. *J. Am. Chem. Soc.* **2008**, *130*, 1676–1680.
- (6) Naya, S.; Inoue, A.; Tada, H. *J. Am. Chem. Soc.* **2010**, *132*, 6292–6293.
- (7) Liu, Z.; Hou, W.; Pavaskar, P.; Aykol, M.; Cronin, S. B. *Nano Lett.* **2011**, *11*, 1111–1116.
- (8) Gomes Silva, C.; Juárez, R.; Marino, T.; Molinari, R.; García, H. *J. Am. Chem. Soc.* **2011**, *133*, 595–602.
- (9) Ingram, D. B.; Linic, S. *J. Am. Chem. Soc.* **2011**, *133*, 5202–5205.
- (10) Tanaka, A.; Hashimoto, K.; Kominami, H. *J. Am. Chem. Soc.* **2012**, *134*, 14526–14533.
- (11) McFarland, E. W.; Tang, J. *Nature* **2003**, *421*, 616–618.
- (12) Furube, A.; Du, L.; Hara, K.; Katoh, R.; Tachiya, M. *J. Am. Chem. Soc.* **2007**, *129*, 14852–14853.
- (13) Du, L.; Furube, A.; Yamamoto, K.; Hara, K.; Katoh, R.; Tachiya, M. *J. Phys. Chem. C* **2009**, *113*, 6454–6462.
- (14) Kowalska, E.; Mahaney, O. O. P.; Abe, R.; Ohtani, B. *Phys. Chem. Chem. Phys.* **2010**, *12*, 2344–2355.
- (15) Nishijima, Y.; Ueno, K.; Yokota, Y.; Murakoshi, K.; Misawa, H. *J. Phys. Chem. Lett.* **2010**, *1*, 2031–2036.
- (16) Ingram, D. B.; Christopher, P.; Bauer, J. L.; Linic, S. *ACS Catal.* **2011**, *1*, 1441–1447.
- (17) Kochuveedu, S. T.; Kim, D.-P.; Kim, D. H. *J. Phys. Chem. C* **2012**, *116*, 2500–2506.
- (18) Seh, Z. W.; Liu, S.; Low, M.; Zhang, S.-Y.; Liu, Z.; Mlayah, A.; Han, M.-Y. *Adv. Mater.* **2012**, *24*, 2310–2314.
- (19) Liu, L.; Ouyang, S.; Ye, J. *Angew. Chem., Int. Ed.* **2013**, *52*, 6689–6693.
- (20) Bian, Z.; Tachikawa, T.; Majima, T. *J. Phys. Chem. Lett.* **2012**, *3*, 1422–1427.
- (21) Bian, Z.; Tachikawa, T.; Kim, W.; Choi, W.; Majima, T. *J. Phys. Chem. C* **2012**, *116*, 25444–25453.
- (22) Li, H.; Bian, Z.; Zhu, J.; Huo, Y.; Li, H.; Lu, Y. *J. Am. Chem. Soc.* **2007**, *129*, 4538–4539.
- (23) Englebienne, P. *Analyst* **1998**, *123*, 1599–1603.
- (24) Prikulis, J.; Hanarp, P.; Olofsson, L.; Sutherland, D.; Kaell, M. *Nano Lett.* **2004**, *4*, 1003–1007.
- (25) Sun, Y.; Xia, Y. *Anal. Chem.* **2002**, *74*, 5297–5305.
- (26) Du, L.; Furube, A.; Hara, K.; Katoh, R.; Tachiya, M. *J. Photochem. Photobiol., C* **2013**, *15*, 21–30.
- (27) Lu, J.; Zhang, P.; Li, A.; Su, F.; Wang, T.; Liu, Y.; Gong, J. *Chem. Commun.* **2013**, *49*, 5817–5819.
- (28) Zhou, N.; Polavarapu, L.; Gao, N.; Pan, Y.; Yuan, P.; Wang, Q.; Xu, Q.-H. *Nanoscale* **2013**, *5*, 4236–4241.
- (29) Tanaka, A.; Sakaguchi, S.; Hashimoto, K.; Kominami, H. *ACS Catal.* **2013**, *3*, 79–85.
- (30) Adleman, J. R.; Boyd, D. A.; Goodwin, D. G.; Psaltis, D. *Nano Lett.* **2009**, *9*, 4417–4423.
- (31) Wang, F.; Li, C.; Chen, H.; Jiang, R.; Sun, L.-D.; Li, Q.; Wang, J.; Yu, J. C.; Yan, C.-H. *J. Am. Chem. Soc.* **2013**, *135*, 5588–5601.
- (32) Vázquez-Vázquez, C.; Vaz, B.; Giannini, V.; Pérez-Lorenzo, M.; Alvarez-Puebla, R. A.; Correa-Duarte, M. A. *J. Am. Chem. Soc.* **2013**, *135*, 13616–13619.
- (33) Tachikawa, T.; Tojo, S.; Fujitsuka, M.; Sekino, T.; Majima, T. *J. Phys. Chem. B* **2006**, *110*, 14055–14059.
- (34) Tachikawa, T.; Yamashita, S.; Majima, T. *J. Am. Chem. Soc.* **2011**, *133*, 7197–7204.

- (35) Furube, A.; Asahi, T.; Masuhara, H.; Yamashita, H.; Anpo, M. *J. Phys. Chem. B* **1999**, *103*, 3120–3127.
- (36) Tachikawa, T.; Fujitsuka, M.; Majima, T. *J. Phys. Chem. C* **2007**, *111*, 5259–5275.
- (37) Yoshihara, T.; Katoh, R.; Furube, A.; Tamaki, Y.; Murai, M.; Hara, K.; Murata, S.; Arakawa, H.; Tachiya, M. *J. Phys. Chem. B* **2004**, *108*, 3817–3823.
- (38) Tamaki, Y.; Furube, A.; Murai, M.; Hara, K.; Katoh, R.; Tachiya, M. *Phys. Chem. Chem. Phys.* **2007**, *9*, 1453–1460.
- (39) Yamakata, A.; Ishibashi, T.; Onishi, H. *J. Phys. Chem. B* **2001**, *105*, 7258–7262.
- (40) Pan, J.; Liu, G.; Lu, G. Q. M.; Cheng, H.-M. *Angew. Chem., Int. Ed.* **2011**, *50*, 2133–2137.
- (41) Gordon, T. R.; Cargnello, M.; Paik, T.; Mangolini, F.; Weber, R. T.; Fornasiero, P.; Murray, C. B. *J. Am. Chem. Soc.* **2012**, *134*, 6751–6761.